Supplementary Information: Cooperative effect of local active stresses on the macroscopic contractility of elastic fiber networks

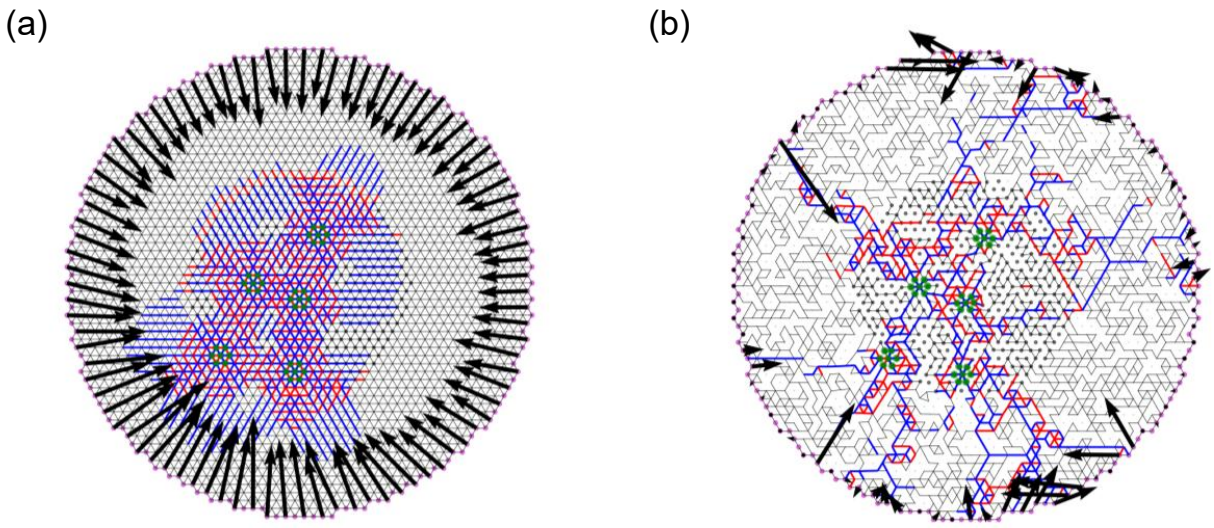

Fig. S1. **Boundary forces for regular and depleted networks.** (a) A network at $p = 1$ and $N_d = 5$. The arrows show boundary forces at fixed boundary nodes, which are averaged over two nearest neighbors for each value shown. The boundary forces all point inwards towards the inner region where all dipoles are placed. Bonds with absolute strains above 10^{-3} are colored in blue (extensile) and red (compressed). (b) Same as (a) but in a network with $p = 0.55$. The arrows, unlike as seen in (a), can point in a variety of directions, including outside the circular region as well due to the randomly depleted network architecture. Many boundary nodes do not have visible arrows as they have negligible forces on them. Bonds with absolute strains above 10^{-7} are colored in blue (extensile) and red (compressed). Both in (a) and (b), the arrow sizes have been normalized by a factor related to the mean boundary forces for each case.

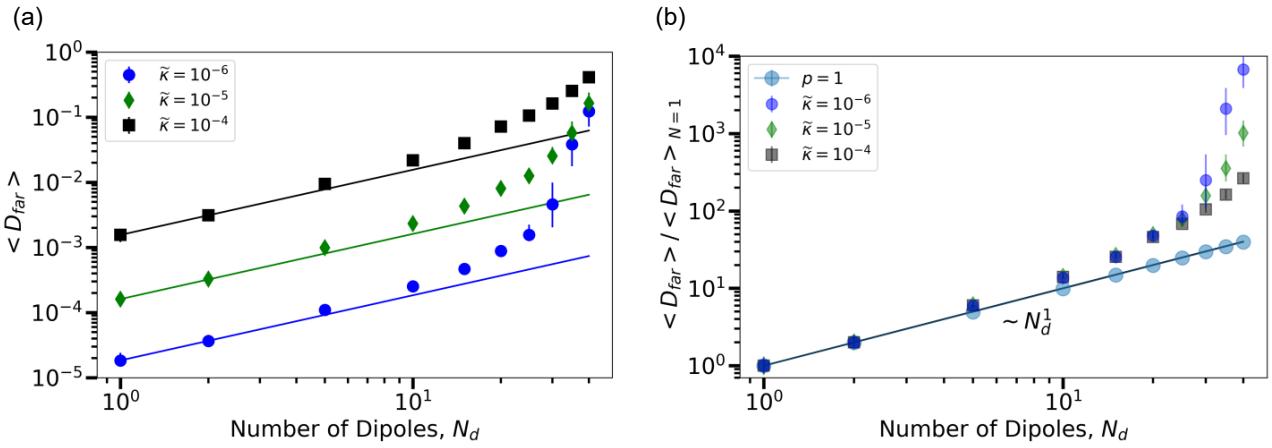

Fig. S2. **Average far field dipole moments of depleted networks of all simulations (including stretching-dominated networks).** (a) Including stretching-dominated results leads to a higher far field dipole moments for $N_d \geq 30$, when compared to Fig. 2a. (b) The inclusion of stretching-dominated networks affects the D_{far} of networks with $\widetilde{\kappa} = 10^{-6}$ the most.

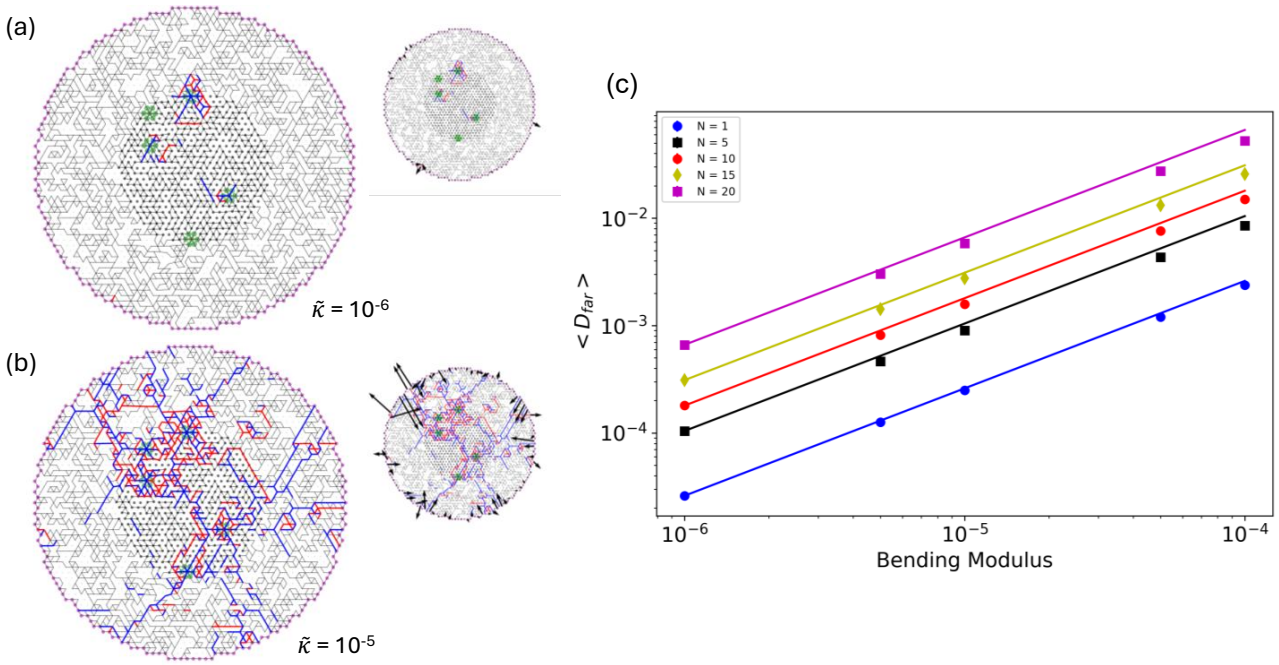

Fig. S3. **Dipole moment at the boundary scales linearly with bending modulus.** (a) Representative image of a network at $p = 0.55$ and $\widetilde{\kappa} = 10^{-6}$ shows almost no force chains. Boundary forces are shown in the inset. (b) Representative image of a network at $p = 0.55$ and $\widetilde{\kappa} = 10^{-5}$ shows many force chains that connect different force dipoles as well as percolate through to the boundaries. Boundary forces are shown in the inset. (c) The average dipole moment at the boundary ($D_{far} = \sum_i \mathbf{f_i} \cdot \mathbf{r_i}$) shows a linear increase with increasing bending modulus. Here, f_i is the normal component of the force on i^{th} node at the boundary. The average was taken over 100 simulations for each value of dipole number and bending modulus.

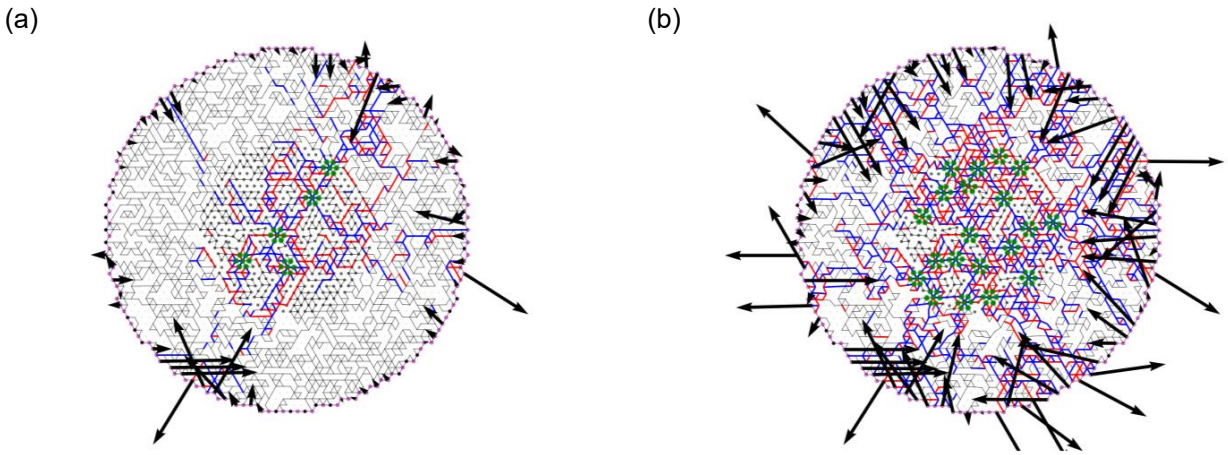

Fig. S4. **The number of highly strained bonds increases with number of dipoles.** (a) Blue (extended) and red (compressed) bonds for a network with 5 dipoles. The bonds above an absolute strain threshold of 10^{-7} are colored in red and blue. (b) When the number of dipoles is 20 in the same network, the highly strained bonds are much greater in number and there are many pathways through which the forces are transmitted to the boundary nodes, leading to a higher value of boundary forces when compared to the $N_d = 5$ case. Boundary forces on alternate boundary nodes are shown by arrows in both (a,b). For visual clarity, arrow lengths are capped at a prescribed maximum value (1.5×10^{-7}).

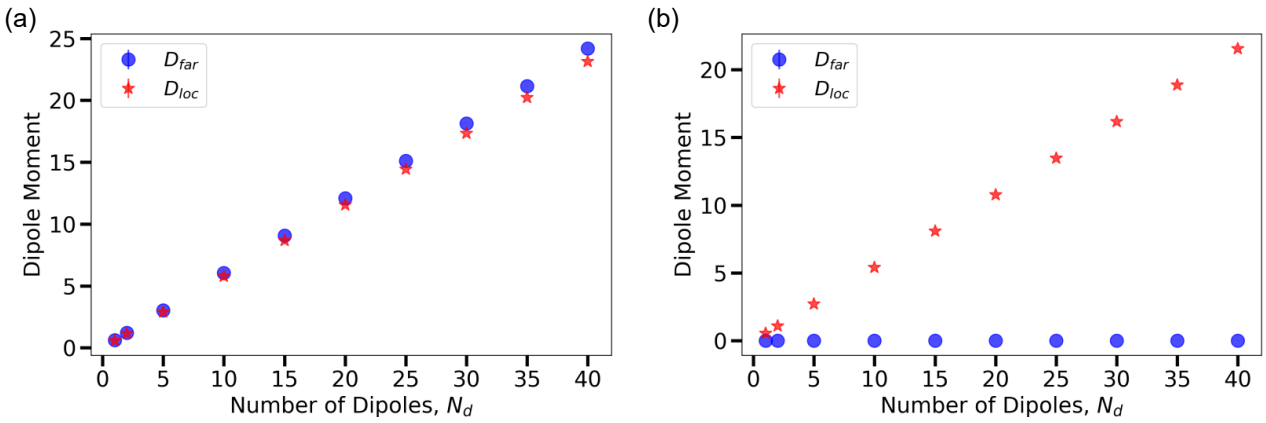

Fig. S5. **Far field dipole moments of depleted networks are much smaller than the corresponding local dipole moments in these networks.** (a) Far field and local dipole moments in a regular network with all bonds present have almost the same values for each dipole number. (b) The far field dipole moment is a small fraction of the corresponding local dipole moment in depleted networks because bending modes screen transmission of forces to the boundary.

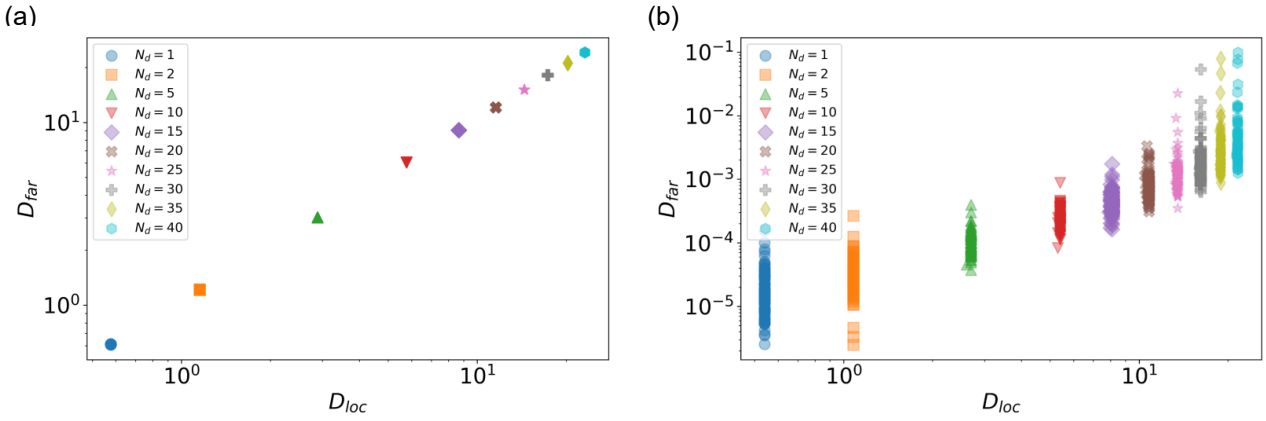

Fig. S6. **Scatter plot of far field dipole moment versus local dipole moment from all simulations shows linear scaling for a fully connected network but a large variance for depleted networks.** (a) The field dipole moment, D_{far} scales linearly with local dipole moment, D_{loc} for a regular network. Both D_{far} and D_{loc} increase with number of dipoles. (b) In contrast, the plot for all the depleted networks (which are bending-dominated) at $p = 0.55$ shows that while D_{far} increases with increasing D_{loc}, it is not linear. Moreover, there is a wide range of variation in the D_{far} value for networks at the same D_{loc}, suggesting that dipole configurations and network architecture could play a role in the propagation of the forces to the boundary.

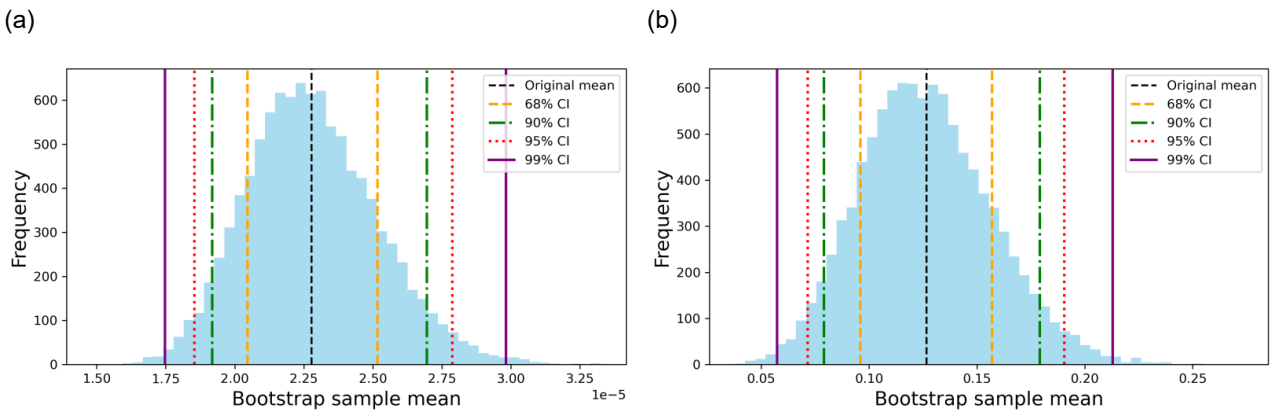

Fig. S7. **Bootstrap resampling (10, 000 resamples) from 100 independent and random simulation realization.** (a,b) Average D_{far} distribution when the original 100 independent simulation realizations were bootstrapped to 10,000 resamples for $N_d = 1$ (a) and $N_d = 40$ (b). The error bars in results in the main text figures were set using the 95% confidence interval values using this method.

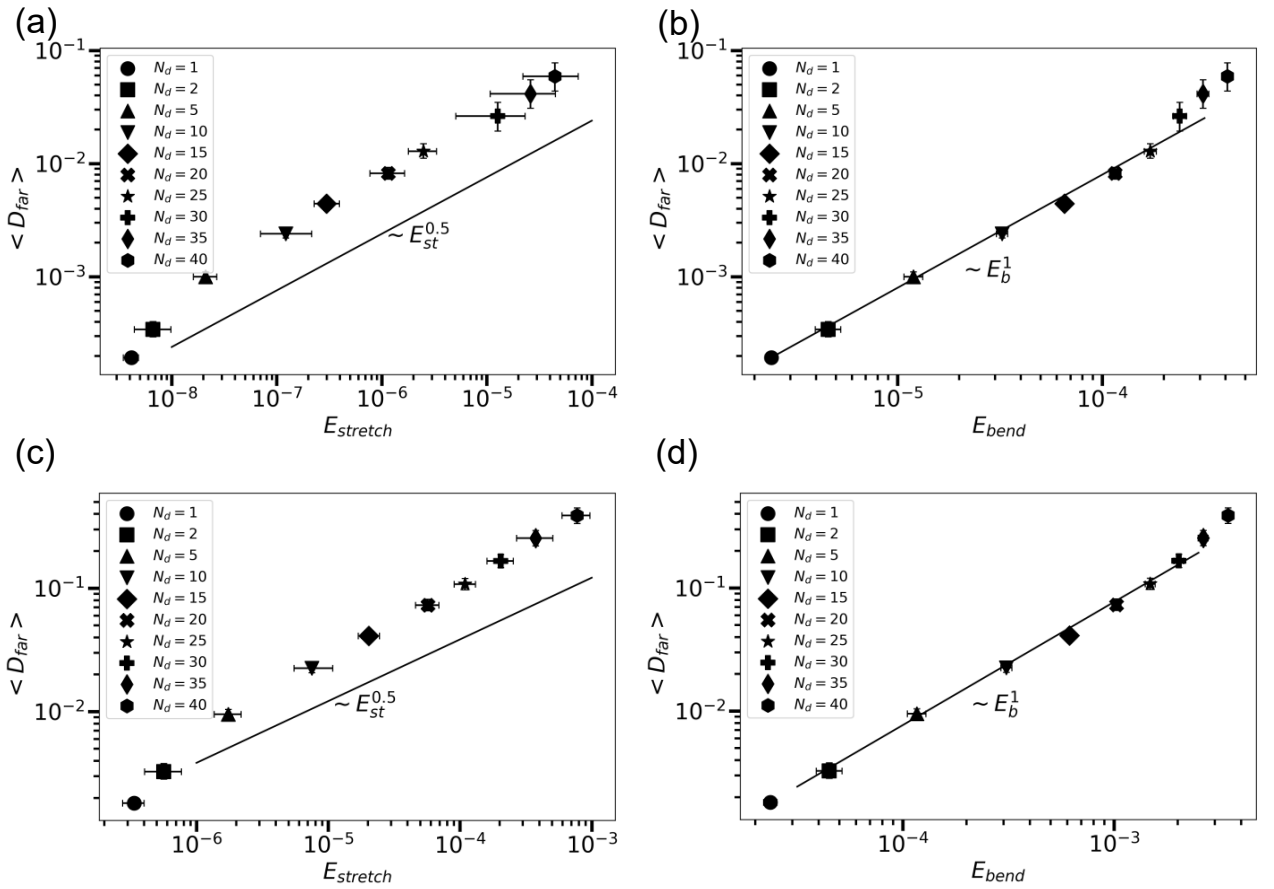

Fig. S8. **Scaling of far field dipole moment with stretching and bending energies at different bending moduli in bending-dominated networks.** (a,b) D_{far} scales as square root of stretching energy and linearly with bending energy in networks with $p = 0.55$ and $\widetilde{\kappa} = 10^{-5}$. (c,d) Similar scaling of the far field dipole moment with stretching and bending energies is also seen when the bending moduli, $\widetilde{\kappa} = 10^{-4}$. Together the results with Fig. 3 in the main text suggest that such a scaling is true in sub-isostatic networks. The error bars denote 95% confidence intervals obtained from bootstrap resampling (10, 000 resamples) from 100 independent simulation realizations for each N_d.

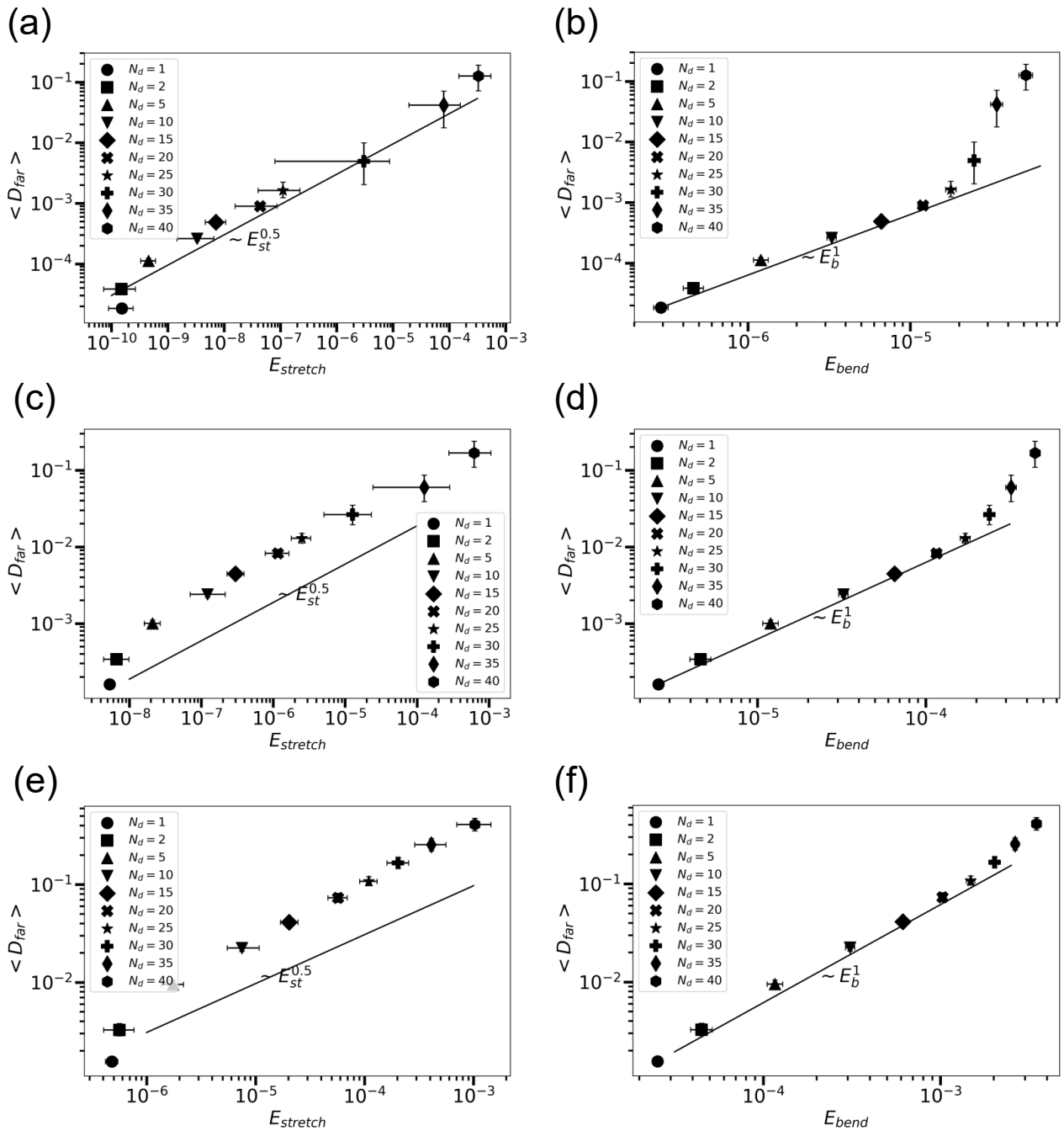

Fig. S9. **Scaling of far field dipole moment with stretching and bending energies at different bending moduli for all network realizations, including stretching-dominated ones.** (a,b) with $p = 0.55$ and $\widetilde{\kappa} = 10^{-6}$. (c,d) with $p = 0.55$ and $\widetilde{\kappa} = 10^{-5}$. (e,f) with $p = 0.55$ and $\widetilde{\kappa} = 10^{-4}$. For comparison, see Fig. 3 in the main text and SI Fig. S8, both of which are based on bending-dominated networks only.

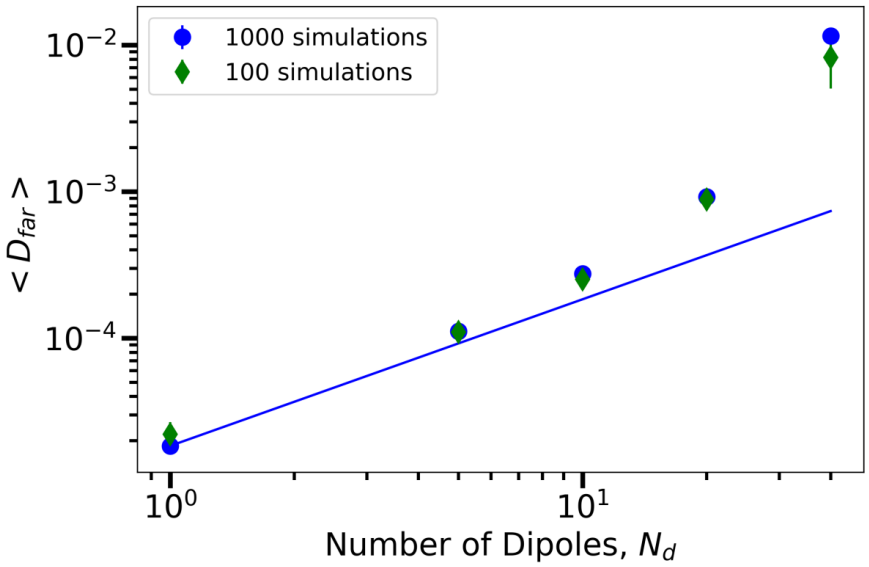

Fig. S10. **Far-field dipole moment averages for 1000 simulations at each N_d agrees with the averages of the original 100 simulations at each N_d.** In the original simulations, for each value of N_d, 10 random dipole placements were chosen and for each random dipole placement, 10 random outer networks were created, which together led to 100 total random simulations. In the new 1000 simulations, 40 random dipole placements were created and for each dipole placement, 25 random outer networks were created for $N_d = 1, 5, 10$. For $N_d = 20, 40$, 10 random dipole placements were chosen and 100 random outer networks were created for each random dipole placement. The error bars here represent a 95% confidence interval. For this analysis, we choose the simulations which were bending-dominated, as we did in our results in Figure 2. These results are for networks at $p = 0.55$ and $\widetilde{\kappa} = 10^{-6}$.

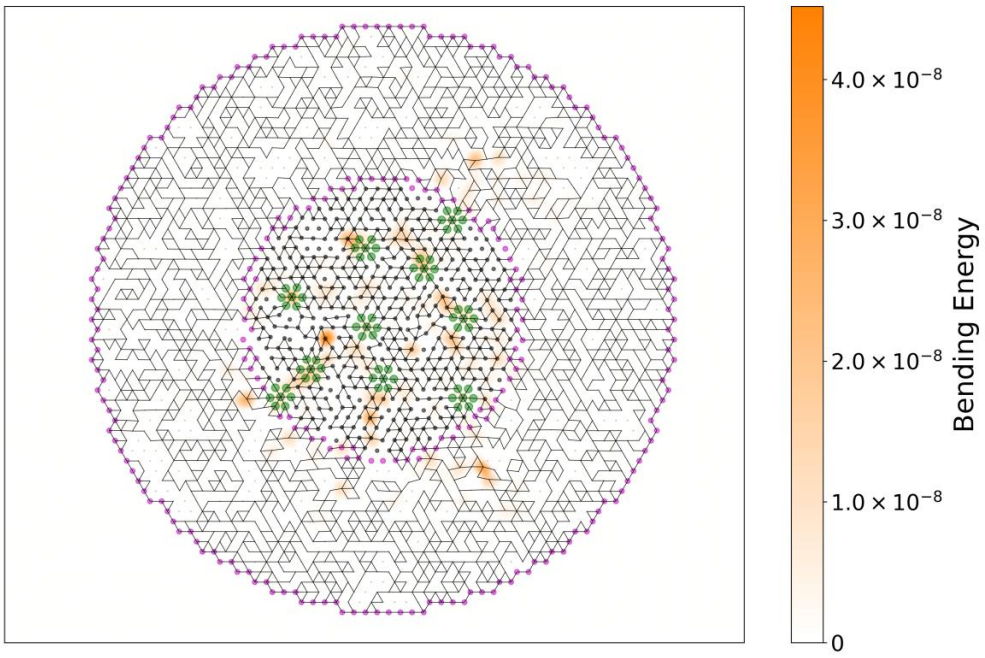

Fig. S11. **Bending regions are dispersed in the network.** Highly bent regions are highlighted using orange and are found dispersed throughout the network, largely near the dipoles but also in regions farther away which may be under-coordinated. The heatmap was produced by using the bending energy at each node and using a cubic spline to smoothen out the discreet values over the $2-$dimensional area. This result is for a 10 dipole network with $p = 0.55$ and $\widetilde{\kappa} = 10^{-6}$.

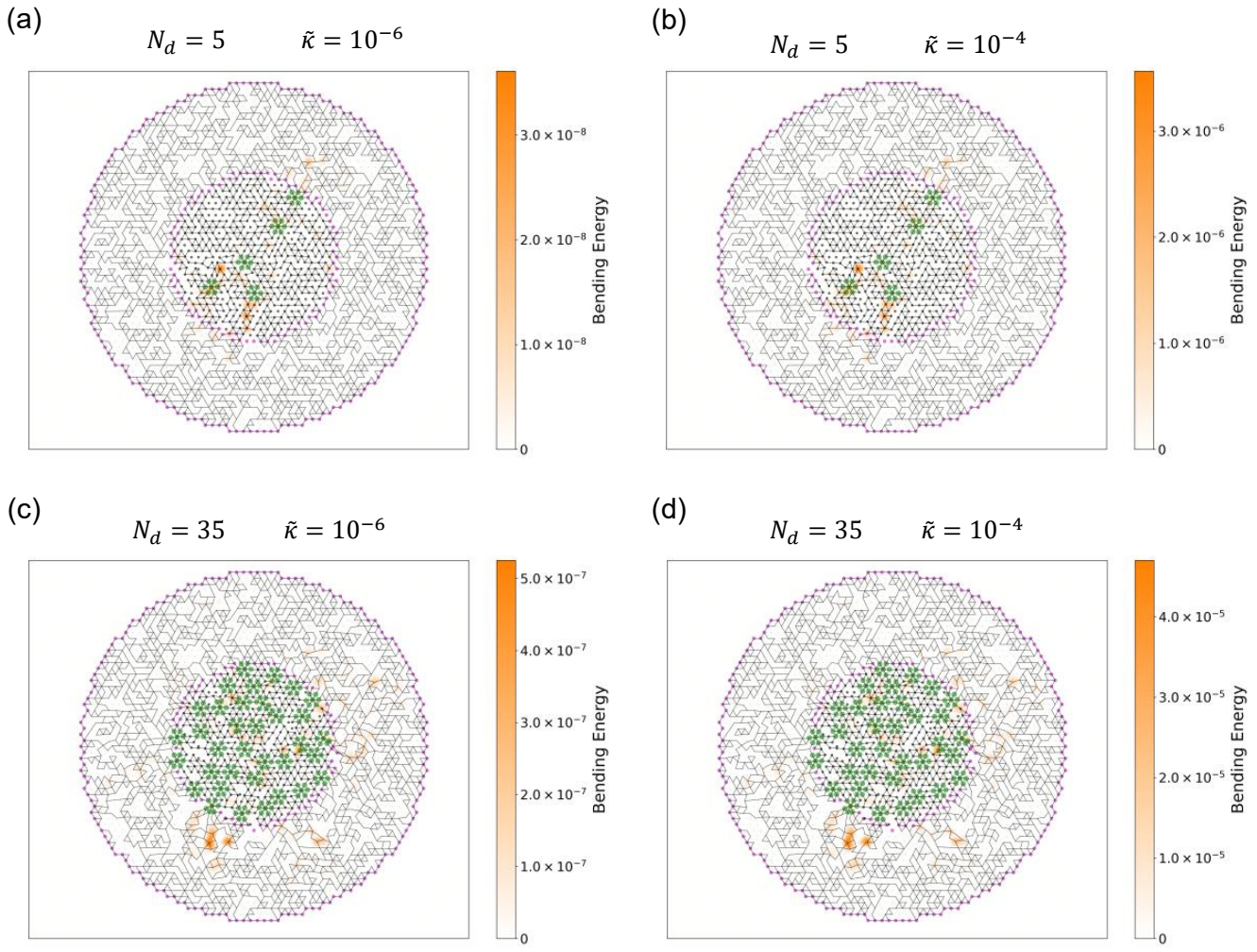

Fig. S12. **Bending modulus scales the bending energy proportionally, but does not change the locations of high bending energies.** (a,b) are bending energy heatmaps for bending moduli $\widetilde{\kappa} = 10^{-6}$ and 10^{-4} respectively. Each network is identical and has 5 dipoles at $p = 0.55$. Highly bent regions are situated at the same locations in both plots, but the magnitude of bending energy stored is about two orders of magnitude higher in (b) than in (a). (c,d) are bending energy heatmaps for bending moduli $\widetilde{\kappa} = 10^{-6}$ and 10^{-4} respectively with $N_d = 35$ and $p = 0.55$ in otherwise identical networks. As seen in (a,b), while the location of high bending energies are the same, their magnitudes differ by a factor similar to that of the bending moduli.

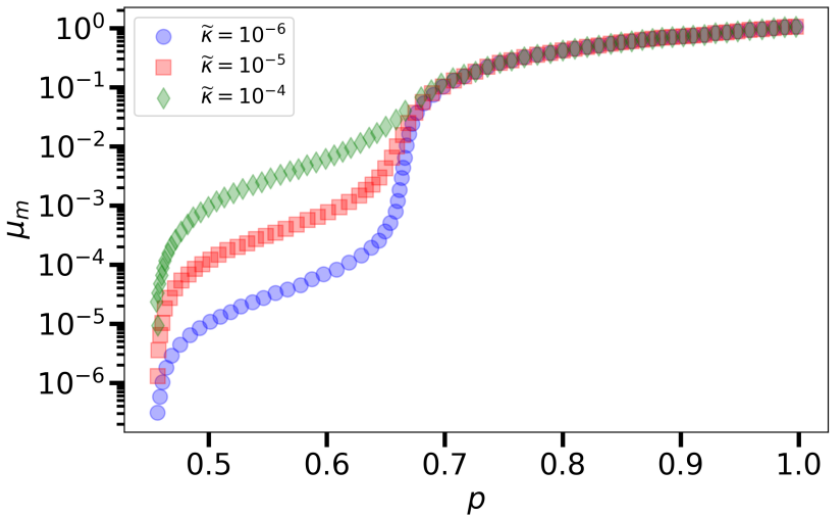

Fig. S13. μ_m **and** p **of an EMT network.** Using this result of the Effective medium theory in Refs. 36, 62 (see main text), and the μ_m values we calculate from boundary forces measured in network simulation, we can read off the p_{eff} value.

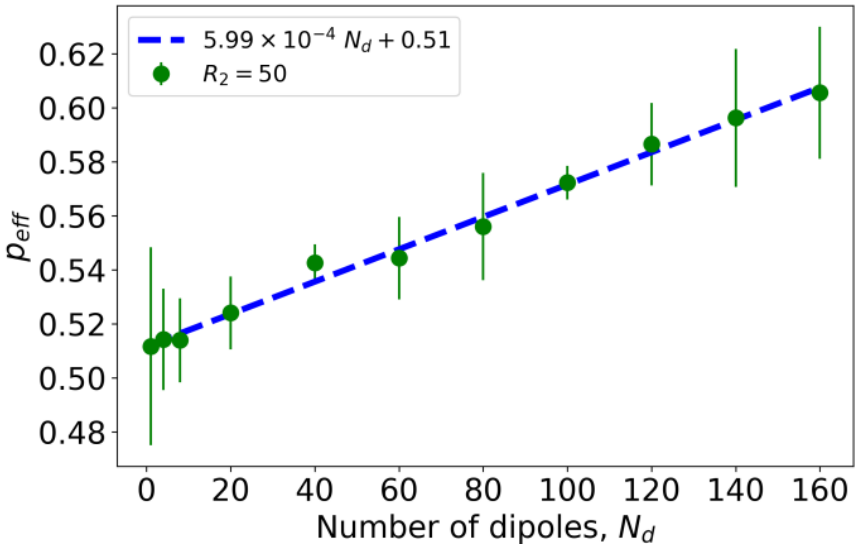

Fig. S14. p_{eff} **scaling with number of dipoles in the larger network with** $R_2 = 50$**.** The ratio of D_{far} at $p = 0.55$ and $p = 1$ gives us μ_m of an EMT network which is then used to get a p_{eff}, similar to that in Fig. 4b (in the main text). The slope of the linear fit is found to be $5.99 \pm 0.27 \times 10^{-4}$. Using constraint counting argument, this gives ~ 17 constraints per dipole, which agrees with the estimate for the smaller network.

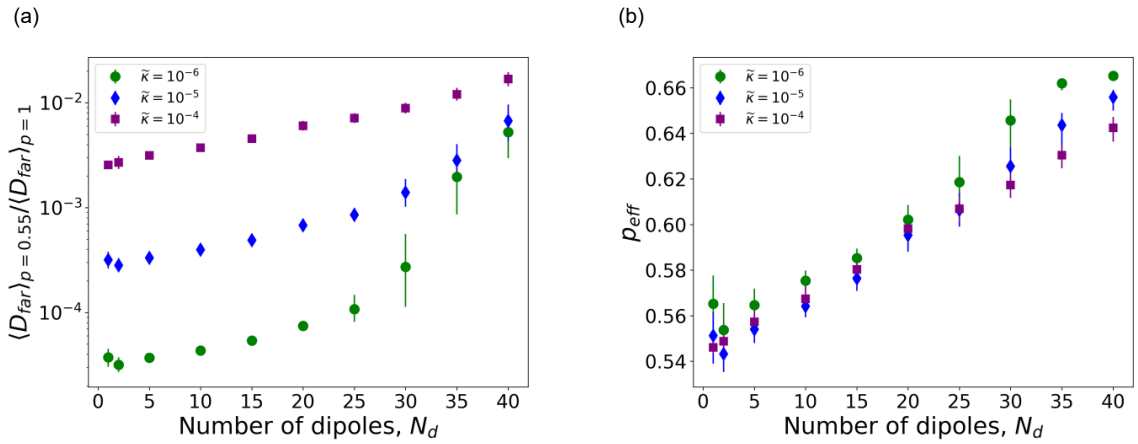

Fig. S15. **Constraint counting in all networks - including stretching-dominated ones.** Counterpart to Fig. 4 in the main text, this figure shows how the effective spring stiffness (a), and the resultant p_{eff} (b) would change if we also included stretching-dominated networks in our analysis.

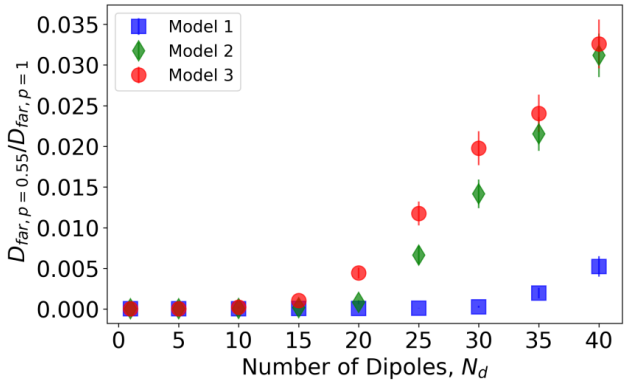

Fig. S16. **The ratio of far-field dipole moments gives us the μ_m of an EMT network for all three models.** Models 2 and 3 have much higher ratios of far field dipole moments when compared to model 1.